Finite-momentum energy dynamics in a Kitaev magnet

Alexandros Metavitsiadis* and Wolfram Brenig†
Institute for Theoretical Physics, Technical University Braunschweig, D-38106 Braunschweig, Germany

(Received 15 March 2021; accepted 30 August 2021; published 24 September 2021)

We study the energy-density dynamics at finite momentum of the two-dimensional Kitaev spin model on the honeycomb lattice. Due to fractionalization of magnetic moments, the energy relaxation occurs through mobile Majorana matter, coupled to a static $\mathbb{Z}_2$ gauge field. At finite temperatures, the $\mathbb{Z}_2$ flux excitations act as a thermally induced disorder, which strongly affects the energy dynamics. We show that sufficiently far above the flux proliferation temperature, but not yet in the high-temperature classical regime, disordered gauge configurations modify the coherent low-temperature energy-density dynamics into a form which is almost diffusive, with a diffusion kernel that is nearly momentum independent, but which remains retarded, primarily due to the presence of two distinct relaxation channels of particle-hole and particle-particle nature. Relations to the thermal conductivity are clarified. Our analysis is based on complementary calculations in the low-temperature homogeneous gauge configuration and a mean-field treatment of thermal gauge fluctuations, valid above the flux proliferation temperature.

DOI: 10.1103/PhysRevB.104.104424

I. INTRODUCTION

Ever since the discovery of large magnetic heat transport in quasi-one-dimensional (quasi-1D) local-moment systems [1–5], the dynamics of energy in quantum magnets [6–8] has been of great interest, since it relates directly to the flow of magnetic energy currents [9–12]. From a fundamental point of view, magnetic thermal transport is a well-established probe into the elementary excitations of magnets and their dissipation [11], which is capable even of revealing topological properties [13]. From an application point of view, spin caloritronics [14,15] and magnetic thermal management devices [16,17] are timely topics. Unfortunately, rigorous theoretical progress has essentially remained confined to one dimension [12]. Above one dimension, understanding energy dynamics in quantum magnets remains an open issue at large. In cases where magnetic long-range order (LRO) is present and magnons form a reliable quasiparticle basis, various insights have been gained for antiferromagnets and cuprates [18–21]. In cases where LRO is absent, and, in particular, in quantum spin liquids (QSLs) [22,23], energy transport has recently come into focus as a probe of potentially exotic elementary excitations. In fact, experiments in several quantum disordered, frustrated spin systems in $D \geqslant 2$ suggest unconventional magnetic energy dynamics. For *bulk* transport, this pertains, e.g., to quasi-2D triangular organic salts [24–26] or to 3D quantum spin ice materials [27–29]. For *boundary* transport, i.e., the magnetic thermal Hall effect, recent examples include kagome magnets [30–32] and spin ice [33]. A microscopic description of such observations is mostly lacking.

In this context, Kitaev's compass exchange Hamiltonian on the honeycomb lattice is of particular interest, as it is one of the few models in which a $\mathbb{Z}_2$ QSL can exactly be shown to exist [13]. The spin degrees of freedom of this model fractionalize in terms of mobile Majorana fermions coupled to a static $\mathbb{Z}_2$ gauge field [13,34–37]. Understanding all of this model's properties may provide insight into other future potential QSLs. From a materials perspective, a realization of the original Kitaev model is lacking as of today, with non-Kitaev exchange being a major obstacle [38]. Among the candidate systems, α-$RuCl_3$ is under intense scrutiny [39]. Free mobile Majorana fermions have been invoked to interpret ubiquitous unconventional continua in spectroscopies on various potential Kitaev materials, such as inelastic neutron [40–42] and Raman scattering [43,44], as well as local resonance probes [45,46].

Majorana fermions should also play a role in the energy dynamics in putative Kitaev materials. However, bulk thermal conductivity, i.e., κ_{xx} in α-$RuCl_3$ [47–50], seems to be governed primarily by phonons, with phonon-Majorana scattering as a potential dissipation mechanism [49,50]. Yet, Majorana fermions may have been observed in the transverse energy conductivity κ_{xy} in magnetic fields, i.e., in the thermal Hall effect, and its alleged quantization with central charge $1/2$ [51,52]. This would render a bosonic origin of the thermal Hall effect in α-$RuCl_3$ unlikely and would be consistent with the behavior at finite fields, of a Kitaev QSL [13], used at zero field in our study.

Dynamical correlation functions of Kitaev QSLs have been at the center of many recent theoretical studies, all of which aim at identifying fingerprints of fractionalized elementary excitations—Majorana fermions and gauge fluxes, and their interaction. Examples include the inelastic spin structure factor [53,54], magnetic Raman scattering [43,55], resonant inelastic x-ray scattering [56], acoustic phonon and ultrasound

*a.metavitsiadis@tu-bs.de
†w.brenig@tu-bs.de

 ©2021 American Physical Society

renormalization [57,58], optical phonon line shapes [59,60], optical conductivity [61], and thermal transport, including the Hall effect [62,63]. See also Ref. [64]. More specifically, these previous investigations of thermal transport have focused on the energy-*current* correlation functions and at *zero momentum* only. In this paper, we take a different perspective and consider the energy-*density* correlation function directly and at finite momentum. In particular, we will be interested in the role which the disorder introduced by thermally excited $\mathbb{Z}_2$ gauge fields plays in the long-wavelength regime. Therefore we map out the energy diffusion kernel of the Kitaev model and its momentum and energy dependence, ranging from low up to intermediate temperatures and we contrast this with expectations for simple diffusion in random systems. We note that the physics of internal "randomness" induced by superselection sectors in *a priori* translationally invariant models of gauge theories is of current interest not only in frustrated magnets [65–67] but also as it relates to questions of many-body localization [68].

The paper is organized as follows. In Sec. II, we briefly recapitulate the Kitaev model and define the observable of interest. In Secs. III A and III B, details of our calculations are provided for the homogeneous and the random gauge configurations. Parts of the technicalities in these sections follow our previous work [57]. The extraction of the diffusion kernel is described in Sec. III C. We discuss our results in Sec. IV, comprising findings on the homogeneous and the random gauge configurations, in Secs. IV A and IV B, respectively. The latter consists of sections on the hydrodynamic description (Sec. IV B 1), generalized Einstein relations (Sec. IV B 2), and the temperature dependence (Sec. IV B 3). We provide a summary in Sec. V. Finally, in Appendix A we detail the finite-size effects, and in Appendix B we present additional results at elevated temperature.

II. MODEL

We consider the Kitaev spin model on the two-dimensional honeycomb lattice

$$H = \sum_{\mathbf{j},\alpha} J_\alpha S^\alpha_{\mathbf{j}} S^\alpha_{\mathbf{j}+\mathbf{r}_\alpha}, \tag{1}$$

where $\mathbf{j} = n_1\mathbf{R}_1 + n_2\mathbf{R}_2$ runs over the sites of the triangular lattice with $\mathbf{R}_{1[2]} = (1, 0)$, $[(\frac{1}{2}, \frac{\sqrt{3}}{2})]$ for lattice constant $a \equiv 1$, and $\mathbf{r}_{\alpha=x,y,z} = (\frac{1}{2}, \frac{1}{2\sqrt{3}})$, $(-\frac{1}{2}, \frac{1}{2\sqrt{3}})$, $(0, -\frac{1}{\sqrt{3}})$ refer to the basis sites $\alpha = x, y, z$, tricoordinated to each lattice site of the honeycomb lattice. We will remain with the isotropic case, i.e., $J_{x,y,z} = J$. As extensive literature, rooted in Ref. [13], has clarified, Eq. (1) can be mapped onto a bilinear form of Majorana fermions in the presence of a static $\mathbb{Z}_2$ gauge field $\eta_{\mathbf{j}} = \pm 1$, residing on, e.g., the z bonds, and its flux $\Phi_{\mathbf{j}} = \eta_{\mathbf{j}}\eta_{\mathbf{j}+\mathbf{R}_1}$

$$H = \sum_{\mathbf{j}} h_{\mathbf{j}}, \quad h_{\mathbf{j}} = -\frac{i}{2}\sum_{\alpha} J\eta_{\mathbf{j},\alpha}\, a_{\mathbf{j}} c_{\mathbf{j}+\mathbf{r}_\alpha}. \tag{2}$$

Here, we introduce $\eta_{\mathbf{j},\alpha}$ to unify the notation, with $\eta_{\mathbf{j},x(y)} = 1$ and $\eta_{\mathbf{j},z} = \eta_{\mathbf{j}}$. There are two types of Majorana particles, corresponding to the two basis sites. We chose to normalize them as $\{a_{\mathbf{j}}, a_{\mathbf{j}'}\} = \delta_{\mathbf{j},\mathbf{j}'}$, $\{c_{\mathbf{m}}, c_{\mathbf{m}'}\} = \delta_{\mathbf{m},\mathbf{m}'}$, and $\{a_{\mathbf{j}}, c_{\mathbf{m}}\} = 0$.

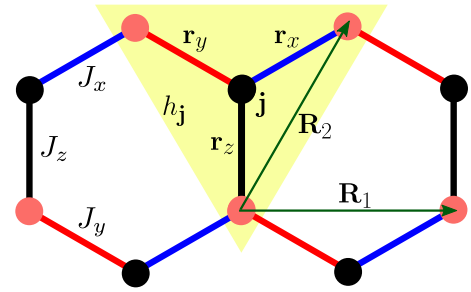

FIG. 1. Kitaev model on the honeycomb lattice. $J_{x,y,z}$ label bond-dependent Ising interactions. $\mathbf{j}$ labels sites of the triangular lattice with lattice vectors $\mathbf{R}_{1,2}$. $\mathbf{r}_{x,y,z}$ label basis sites. The yellow triangle comprises sites and bonds of the local energy density $h_{\mathbf{j}}$.

For each gauge configuration, i.e., set of $\{\eta_{\mathbf{j}}\}$, the fermionic Hilbert space of Eq. (2), the so-called gauge sector, represents a spin liquid.

To study the energy-density susceptibility, a local energy density $\tilde{h}_{\mathbf{u}}$ on some repeating "unit" cluster $\mathbf{u}$ has to be chosen. Obviously, the sum over all units of these local energy densities should equal the total Hamiltonian, $H = \sum_{\mathbf{u}} \tilde{h}_{\mathbf{u}}$. As for any local density, the latter does not fix $\tilde{h}_{\mathbf{u}}$ uniquely. Different shapes of the real-space units $\mathbf{u}$ supporting $\tilde{h}_{\mathbf{u}}$ will typically lead to differing high-frequency and short-wavelength spectra for its autocorrelation function [69]. However the low-frequency, long-wavelength dynamics is governed by energy conservation and will not depend on a particular choice of $\tilde{h}_{\mathbf{u}}$ [69]. For the remainder of this paper we therefore set $\tilde{h}_{\mathbf{u}} = h_{\mathbf{j}}$, with $h_{\mathbf{j}}$ defined in Eq. (2), i.e., the energy density formed by the tricoordinated bonds around each site on the triangular lattice, highlighted by the yellow triangle in Fig. 1. Its Fourier transform is $h_{\mathbf{q}} = \sum_{\mathbf{j}} e^{i\mathbf{q}\cdot\mathbf{j}} h_{\mathbf{j}}$ with $h^\dagger_{\mathbf{q}} = h_{-\mathbf{q}}$ and $h_{\mathbf{0}} = H$.

III. ENERGY SUSCEPTIBILITY

In this section, we present our evaluation of the dynamical energy susceptibility. The approach parallels our previous work on phonon self-energies [57]. For the sake of completeness, however, we repeat the steps necessary for the present calculation. We focus on two temperature regimes, namely, $T \lesssim T^\star$ and $T \gtrsim T^\star$. Here, $T^\star$ is the so-called flux proliferation temperature. Well below $T^\star$, the gauge field is in an ordered uniform configuration, i.e., $\eta_{\mathbf{j}} = 1$, $\forall \mathbf{j}$. Here, flipping a gauge field involves an energy cost, the so-called flux gap $\Delta \approx 0.065J$ [13]. In the vicinity of $T^\star$, other gauge field or flux configurations get thermally populated [61,70]. This means that mostly gauge field configurations are present, which no longer conform with translation invariance. These gauge field configurations act as a thermally induced disorder, modifying the environment in which the Majorana fermions move at all temperatures well above $T^\star$. Previous analysis [61,63,69,70] has shown that the temperature range over which a *complete* proliferation of fluxes occurs is confined to a rather narrow region—less than a decade centered around $T^\star \approx 0.012J$ for the isotropic exchange used in this paper—which decreases rapidly with anisotropy [61,70]. Our strategy therefore is to consider a homogeneous gauge configuration, i.e., $\eta_{\mathbf{j}} = 1$ for $T \lesssim T^\star$ and an average over a sufficiently large

number of completely random gauge configurations for $T \gtrsim T^\star$. For brevity we call this the "random gauge (configuration)" hereafter. In the latter case, the ensemble average of the gauge field vanishes, $\langle \eta_{\mathbf{j}} \rangle = 0$. This approach has proven to work very well on a *quantitative* level in several studies of the thermal conductivity of Kitaev models [63,70,71]. Note that for α-$RuCl_3$, and assuming only a plain Kitaev magnet, with a Kitaev exchange, generally accepted to be $|J| \sim 85$ K [40], the study of $T \lesssim T^\star$ requires temperatures well below the boiling point of liquid helium-4. Access to $T \gtrsim T^\star$ therefore requires less effort.

A. Homogeneous gauge: $T \lesssim T^\star$

For $\eta_{\mathbf{j}} = 1$, the Hamiltonian (1) can be diagonalized *analytically* in terms of complex Dirac fermions. Mapping from the real Majorana fermions to the latter can be achieved in various ways, all of which require some type of linear combination of real fermions in order to form complex ones. Here, we do the latter by using Fourier-transformed Majorana particles, $a_{\mathbf{k}} = \sum_{\mathbf{j}} e^{-i\mathbf{k}\cdot\mathbf{j}} a_{\mathbf{j}}/\sqrt{N}$ with momentum $\mathbf{k}$ and analogously for $c_{\mathbf{k}}$. The momentum-space quantization is chosen explicitly to comprise $\pm\mathbf{k}$ for each $|\mathbf{k}|$. Other approaches, involving reshaped lattice structures [34,36], may pose issues regarding the discrete rotational symmetry of the susceptibility.

The fermions introduced in momentum space are complex with $a^\dagger_{\mathbf{k}} = a_{-\mathbf{k}}$, i.e., with only half of the momentum states being independent. This encodes that for each Dirac fermion there are two Majorana particles. Standard anticommutation relations apply, $\{a_{\mathbf{k}}, a^\dagger_{\mathbf{k}'}\} = \delta_{\mathbf{k},\mathbf{k}'}$, $\{c_{\mathbf{k}}, c^\dagger_{\mathbf{k}'}\} = \delta_{\mathbf{k},\mathbf{k}'}$, and $\{a^{(\dagger)}_{\mathbf{k}} c^{(\dagger)}_{\mathbf{k}'}\} = 0$. From this, the diagonal form of H reads

$$H = \tilde{\sum_{\mathbf{k},\gamma=1,2}} \mathrm{sg}_\gamma \, \epsilon_{\mathbf{k}} \, d^\dagger_{\mathbf{k},\gamma} d_{\mathbf{k},\gamma}, \tag{3}$$

where the $\sim$ implies summing over a suitably chosen "positive" half of momentum space and $\mathrm{sg}_\gamma = 1$ (-1) for $\gamma = 1$ (2). The quasiparticle energy is $\epsilon_{\mathbf{k}} = J[3 + 2\cos(k_x) + 4\cos(k_x/2)\cos(\sqrt{3}k_y/2)]^{1/2}/2$. In terms of reciprocal lattice coordinates $x, y \in [0, 2\pi]$, this reads $\epsilon_{\mathbf{k}} = J[3 + 2\cos(x) + 2\cos(y) + 2\cos(x-y)]^{1/2}/2$ with $\mathbf{k} = x\,\mathbf{G}_1 + y\,\mathbf{G}_2$, where $\mathbf{G}_{1[2]} = (1, -\frac{1}{\sqrt{3}})$, $[(0, \frac{2}{\sqrt{3}})]$. The quasiparticles are given by

$$\begin{bmatrix} c_{\mathbf{k}} \\ a_{\mathbf{k}} \end{bmatrix} = \begin{bmatrix} u_{11}(\mathbf{k}) & u_{12}(\mathbf{k}) \\ u_{21}(\mathbf{k}) & u_{22}(\mathbf{k}) \end{bmatrix} \begin{bmatrix} d_{1\mathbf{k}} \\ d_{2\mathbf{k}} \end{bmatrix},$$
$$u_{11}(\mathbf{k}) = -u_{12}(\mathbf{k}) = \frac{i\sum_\alpha e^{-i\mathbf{k}\cdot\mathbf{r}_\alpha}}{2^{3/2}\epsilon_{\mathbf{k}}}, \tag{4}$$
$$u_{21}(\mathbf{k}) = u_{22}(\mathbf{k}) = \frac{1}{\sqrt{2}}.$$

From the sign change of the quasiparticle energy between bands $\gamma = 1$ and $\gamma = 2$ in Eq. (3) it is clear that the relations $a^\dagger_{\mathbf{k}} = a_{-\mathbf{k}}$ and $c^\dagger_{\mathbf{k}} = c_{-\mathbf{k}}$ for reversing momenta of the original Majorana fermions have to change into $d^\dagger_{1(2)\mathbf{k}} = d_{2(1)-\mathbf{k}}$, switching also the bands. Indeed this is also born out of the transformation (4). Inserting the latter into $h_{\mathbf{q}}$, the energy density in the quasiparticle basis reads

$$h_{\mathbf{q}} = \frac{1}{2}\tilde{\sum_{\mathbf{k}}} \Big\{ [d^\dagger_{1\mathbf{k}+\mathbf{q}} \quad d^\dagger_{2\mathbf{k}+\mathbf{q}}] \times \begin{bmatrix} \epsilon_{\mathbf{k}+\mathbf{q}}+\epsilon_{\mathbf{k}} & \epsilon_{\mathbf{k}+\mathbf{q}}-\epsilon_{\mathbf{k}} \\ \epsilon_{\mathbf{k}}-\epsilon_{\mathbf{k}+\mathbf{q}} & -\epsilon_{\mathbf{k}+\mathbf{q}}-\epsilon_{\mathbf{k}} \end{bmatrix} \begin{bmatrix} d_{1\mathbf{k}} \\ d_{2\mathbf{k}} \end{bmatrix} \Big\}. \tag{5}$$

As is to be expected, $h_{\mathbf{q}=\mathbf{0}} = H$ from (3), and the off-diagonal interband transitions vanish in that limit.

The energy-density susceptibility $\chi(\mathbf{q}, z)$ is obtained from Fourier transformation of the imaginary time density Green's function $\chi(\mathbf{q}, z) = T\int_0^\beta d\tau \langle T_\tau(h_{\mathbf{q}}(\tau)h_{-\mathbf{q}})\rangle e^{i\omega_n\tau}$ by analytic continuation of the Bose Matsubara frequency $i\omega_n = i2\pi nT \to z \in \mathbb{C}$ and eventually $z \to \omega + i0^+$. While the physical momentum of the density $\mathbf{q}$ is an element of all of the Brillouin zone (BZ) of the honeycomb lattice, due to the mutual dependence of the fermions, and as discussed directly before Eq. (3), the momentum $\mathbf{k}$ is *a priori* restricted to only a suitably chosen positive half of the BZ. This seems to complicate evaluation of $\chi(\mathbf{q}, z)$ but can readily be simplified by allowing $\mathbf{k}$ sums run over all of the BZ. This implies a double counting, which can be corrected for by appropriate factors of $1/2$, and more important, this comes at the expense of additional anomalous anticommutators such as, e.g., $\{d_{1\mathbf{k}}, d_{2\mathbf{k}'}\} = \delta_{-\mathbf{k},\mathbf{k}'}$ and their corresponding contractions. Simple algebra yields [72]

$$\chi(\mathbf{q}, z) = \chi^{\mathrm{ph}}(\mathbf{q}, z) + \chi^{\mathrm{pp}}(\mathbf{q}, z),$$
$$\chi^{\mathrm{ph}}(\mathbf{q}, z) = \frac{1}{N}\sum_{\mathbf{k}} (\epsilon_{\mathbf{k}+\mathbf{q}}+\epsilon_{\mathbf{k}})^2 \frac{f_{\mathbf{k}+\mathbf{q}}(T) - f_{\mathbf{k}}(T)}{z - \epsilon_{\mathbf{k}+\mathbf{q}} + \epsilon_{\mathbf{k}}},$$
$$\chi^{\mathrm{pp}}(\mathbf{q}, z) = \frac{1}{2N}\sum_{\mathbf{k}} (\epsilon_{\mathbf{k}+\mathbf{q}}-\epsilon_{\mathbf{k}})^2 \{[f_{\mathbf{k}+\mathbf{q}}(T) + f_{\mathbf{k}}(T) - 1] \times \left(\frac{1}{z - \epsilon_{\mathbf{k}+\mathbf{q}} - \epsilon_{\mathbf{k}}} - \frac{1}{z + \epsilon_{\mathbf{k}+\mathbf{q}} + \epsilon_{\mathbf{k}}}\right)\Big\}, \tag{6}$$

where the superscripts ph (pp) indicate particle-hole (particle-particle), or the synonymous intraband (interband), types of intermediate states of the fermions; $f_{\mathbf{k}}(T) = 1/(e^{\epsilon_{\mathbf{k}}/T} + 1)$ is the Fermi function. This concludes the formal details for $T \lesssim T^\star$.

B. Random gauge: $T \gtrsim T^\star$

In a random gauge configuration, translational invariance of the Majorana system is lost, and we resort to a numerical approach in real space. This has been detailed extensively for 1D [69,71] and 2D [57,63,70] models and is only briefly reiterated here for the sake of completeness. First a spinor $A^\dagger_\sigma = (a_1 \cdots a_{\mathbf{j}} \cdots a_N,\ c_1 \cdots c_{\mathbf{j}+\mathbf{r}_x} \cdots c_N)$, comprising the Majorana fermions on the $2N$ sites of the lattice, is defined. Using this, the energy density $h_{\mathbf{q}}$ and the Hamiltonian (2), i.e., $h_{\mathbf{0}}$, are rewritten as $h_{\mathbf{q}} = \mathbf{A}^\dagger \mathbf{g}_{\mathbf{q}} \mathbf{A}/2$. Boldfaced symbols refer to vectors and matrices, i.e., $\mathbf{g}_{\mathbf{q}}$ is a $2N \times 2N$ array. Next a spinor $D^\dagger_\sigma = (d^\dagger_1 \cdots d^\dagger_N, d_1 \cdots d_N)$ of $2N$ complex fermions is defined by $\mathbf{D} = \mathbf{F}\mathbf{A}$ using the unitary (Fourier) transform $\mathbf{F}$. The latter is built from two disjoint $N \times N$ blocks $I^{i=1,2}_{\sigma\rho} = e^{-i\mathbf{k}_\sigma \cdot \mathbf{R}^i_\rho}/\sqrt{N}$, with $\mathbf{R}^i_\rho = \mathbf{j}$ and $\mathbf{j} + \mathbf{r}_x$, for a- and c-Majorana lattice sites, respectively. $\mathbf{k}$ is chosen such that for each $\mathbf{k}$ there

exists one $-\mathbf{k}$, with $\mathbf{k} \neq -\mathbf{k}$. Finally, for convenience, $\mathbf{F}$ is rearranged so as to associate the $d_1^\dagger \cdots d_N^\dagger$ with the $2\,(N/2) = N$ "positive" $\mathbf{k}$ vectors. With this,

$$h_\mathbf{q} = \mathbf{D}^\dagger \tilde{\mathbf{g}}_\mathbf{q} \mathbf{D}/2, \tag{7}$$

where $\tilde{\mathbf{o}} = \mathbf{F}\mathbf{o}\mathbf{F}^\dagger$. We emphasize that (i) $\mathbf{F}$ does *not* diagonalize $h_\mathbf{q}$ and (ii) in general the $2N \times 2N$ matrices of Fourier-transformed operators $\tilde{\mathbf{o}}$ will contain particle number nonconserving entries of $\mathbf{D}$ fermions.

As for the case of the homogeneous gauge in Sec. III A, the energy-density susceptibility $\chi(\mathbf{q}, z)$ for a *particular* gauge configuration $\{\eta_\mathbf{j}\}$ is obtained by analytic continuation from the imaginary time density Green's function

$$\begin{aligned}\chi(\mathbf{q}, \tau) &= \langle T_\tau (h_\mathbf{q}(\tau) h_{-\mathbf{q}}) \rangle_{\{\eta_\mathbf{j}\}} \\ &= \tfrac{1}{4} \langle T_\tau [(\mathbf{D}^\dagger \tilde{\mathbf{g}}_\mathbf{q} \mathbf{D})(\tau)(\mathbf{D}^\dagger \tilde{\mathbf{g}}_\mathbf{q} \mathbf{D})^\dagger] \rangle_{\{\eta_\mathbf{j}\}}. \end{aligned} \tag{8}$$

This is evaluated using Wick's theorem for quasiparticles $\mathbf{T} = \mathbf{U}\mathbf{D}$, referring to a $2N \times 2N$ Bogoliubov transformation $\mathbf{U}$, determined numerically for a given distribution $\{\eta_\mathbf{j}\}$, so as to diagonalize $\tilde{\mathbf{g}}_\mathbf{0}$, i.e., $(\mathbf{U}\tilde{\mathbf{g}}_\mathbf{0}\mathbf{U}^\dagger)_{\rho\sigma} = \delta_{\rho\sigma}\epsilon_\rho$, with $\epsilon_\rho = (\epsilon_1 \cdots \epsilon_N, \, -\epsilon_1 \cdots -\epsilon_N)$. We get

$$\begin{aligned}\chi(\mathbf{q}, z) &= \sum_{\rho\sigma} \Pi_{\sigma\rho}(z) w_{\sigma\rho,\mathbf{q}} [w^\star_{\bar{\rho}\bar{\sigma},\mathbf{q}} - w^\star_{\sigma\rho,\mathbf{q}}], \\ \Pi_{\sigma\rho}(z) &= \frac{f_\sigma(T) - f_\rho(T)}{z - \epsilon_\sigma + \epsilon_\rho}, \\ w_{\rho\sigma,\mathbf{q}} &= \left(\frac{1}{2}\mathbf{U}\tilde{\mathbf{g}}_\mathbf{q}\mathbf{U}^\dagger\right)_{\rho\sigma}, \end{aligned} \tag{9}$$

where $f_\sigma(T) = 1/(e^{\epsilon_\sigma/T} + 1)$ and overbars refer to swapping the upper and lower half of the range of $2N$ indices, e.g., $\bar{\rho} = \rho \mp N$ for $\rho \gtrless N$ [72].

As a final step, $\chi(\mathbf{q}, z)$ from Eq. (9) is averaged over a sufficiently large number of random gauge configurations $\{\eta_\mathbf{j}\}$. For the numerical evaluations in this paper, we average over 200 such random realizations and—for brevity—refer to this average simply as the random gauge (configuration) hereafter. We have tested that this is fully sufficient to have negligible stochastic errors on the system sizes we use (see Appendix A). This concludes the formal details of the evaluation of the energy-density susceptibility for $T \gtrsim T^\star$.

C. Diffusion kernel

We will relate $\chi(\mathbf{q}, z)$ to a diffusion kernel $D(\mathbf{q}, z)$ by the following phenomenological ansatz, rooted in hydrodynamic theory and memory function approaches [73]:

$$\chi(\mathbf{q}, \omega) = \chi_\mathbf{q} \frac{iq^2 D(\mathbf{q}, \omega)}{\omega + iq^2 D(\mathbf{q}, \omega)}. \tag{10}$$

For the remainder of this paper, only the real part, i.e., ω, of the frequency argument z of causal functions is displayed, and an infinitesimal positive imaginary part, i.e., broadening, $\mathrm{Im}(z) = i0^+$ is implied [74].

Equation (10) should be viewed as a definition of $D(\mathbf{q}, \omega)$ and a static energy-density susceptibility $\chi_\mathbf{q}$. This neither takes into account fine details concerning differences between static, adiabatic, and isolated susceptibilities nor formulates the momentum scaling in terms of harmonics of the honeycomb lattice instead of the simpler factor of q^2. The latter implies that the momentum dependence of $D(\mathbf{q}, \omega)$ is adapted best to the small-q regime. We denote the damping rate $q^2 D(\mathbf{q}, \omega)$ to satisfy perfect q^2 scaling, if $D(\mathbf{q}, \omega)$ is momentum independent, meaning that momentum enters the density relaxation solely by the q scaling of the gradient in the continuity equation, leading to a simple Fick's law with respect to q.

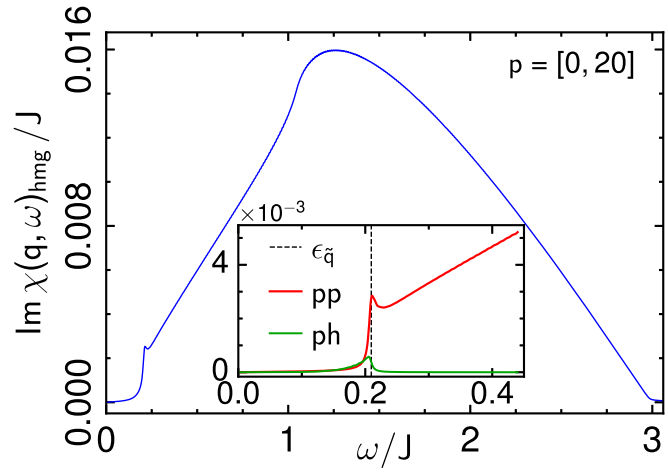

FIG. 2. Spectrum, $\mathrm{Im}\,\chi(\mathbf{q}, \omega)$, of energy-density susceptibility vs ω at fixed small $\mathbf{q}$ set by p, for low $T = 0.01J \lesssim T^\star$, using Eq. (6) for the homogeneous (hmg) gauge configuration. System size is $L^2 = 300 \times 300$. Inset: Blowup of the low-ω region, separating ph (green) and pp spectra (red), with the dashed vertical line showing the upper ph-continuum bound at $\mathbf{q}$.

Since, by construction of (10), $D(\mathbf{q}, \omega)$ has a proper spectral representation, $\chi_\mathbf{q}$ results from the sum rule

$$\chi_\mathbf{q} = \int_{-\infty}^{\infty} \frac{d\omega}{\pi\omega} \mathrm{Im}[\chi(\mathbf{q}, \omega)]. \tag{11}$$

Introducing a normalized susceptibility $\bar{\chi}(\mathbf{q}, \omega) = \chi(\mathbf{q}, \omega)/\chi_\mathbf{q}$, we will extract the diffusion kernel from

$$D(\mathbf{q}, \omega) = \frac{1}{iq^2} \frac{\omega\, \bar{\chi}(\mathbf{q}, \omega)}{1 - \bar{\chi}(\mathbf{q}, \omega)}. \tag{12}$$

IV. RESULTS

A. Homogeneous gauge: $T \lesssim T^\star$

We now discuss the density dynamics as obtained from the previous sections. First we consider the low-T behavior, $T \lesssim T^\star$, using the homogeneous gauge configuration. As from Eq. (6), $\chi(\mathbf{q}, \omega)$ sums two channels: (i) particle-hole (ph) and (ii) particle-particle (pp) excitations. Their spectral support is $0 < |\omega| < \epsilon_{\tilde{\mathbf{q}}}$ for ph and $\epsilon_{\tilde{\mathbf{q}}} < |\omega| \lesssim \max(2\epsilon_\mathbf{k}) = 3J$ at $|\mathbf{q}| \ll 1$ for pp, where $\tilde{\mathbf{q}} = \mathbf{q} + \mathbf{k}_D$ refers to the wave vector with respect to the location of the Dirac cone.

A typical spectrum $\mathrm{Im}\,\chi(\mathbf{q}, \omega)$ is shown in Fig. 2 at small, albeit finite $\mathbf{q}$. For the remainder of this paper, we label the discrete momenta of the BZ of the finite 2D lattice in terms of integer doublets $p = [p_1, p_2]$, with respect to the reciprocal lattice vectors, i.e., $\mathbf{q} = 2\pi \sum_{i=1,2} \mathbf{G}_i p_i / L$. The inset of

Fig. 2 depicts a blowup of the low-ω region separating the spectrum into its ph and pp contributions. While the imaginary broadening in this plot is chosen such that finite-size oscillations are acceptably small, the pp channel still exhibits some weight below its cutoff at $\epsilon_{\tilde{\mathbf{q}}} \simeq 0.208J$. This will vanish for vanishing imaginary broadening, however, at the expense of larger finite-size oscillations. For the ph channel, the spectral weight in this energy range is related to the Fermi sea of the complex fermions. Due to the Dirac cone, the Fermi volume shrinks to zero in the Kitaev model as $T \to 0$, i.e., occupied states only stem from a small patch with $\epsilon_{\mathbf{k}} \lesssim T$ around the Dirac cone. Therefore the weight of the ph channel decreases rapidly to zero as $T \to 0$. In this regime and for small $\mathbf{q}$, because of the linear fermion dispersion close to the cones, only a narrow strip of order $\omega \in [\max(0, \epsilon_{\tilde{\mathbf{q}}} - 2T), \epsilon_{\tilde{\mathbf{q}}}]$ from the spectral support dominates the ph continuum. At the upper edge of its support the ph DOS is singular. The inset of Fig. 2 is consistent with this, considering the finite system size and imaginary broadening.

Regarding the pp channel, the complete two-particle continuum is unoccupied and available for excited states as $T \to 0$. This leads to the broad spectral hump seen in Fig. 2, which extends out to $\max(2\epsilon_{\mathbf{k}}) = 3J$ and is two orders of magnitude larger than the ph process at this temperature.

A fingerprint of potentially diffusive relaxation of density modes at finite momentum $\mathbf{q}$ is the near-linear behavior of $\mathrm{Im}\chi(\mathbf{q}, \omega) \sim \chi_{\mathbf{q}}\,\omega/(Dq^2)$ at small ω. Definitely, neither should this be expected, nor is it observed in Fig. 2, since for $T \lesssim T^\star$ the density dynamics is set by coherent two-particle excitations of the Dirac fermions in the homogeneous gauge configuration.

B. Random gauge: $T \gtrsim T^\star$

Now we turn to temperatures above the flux proliferation, i.e., $T \gtrsim T^\star$, using random gauge configurations. To begin, we first describe the impact of the random gauge by contrasting the dynamic density susceptibilities against each other with and without the random gauge, for otherwise identical system parameters and for two different temperatures, $T/J = 0.1$ and 0.5, in Figs. 3(a) and 3(c), and Figs. 3(b) and 3(d), respectively. Note, that while the linear system size is smaller by a factor of 5 with respect to Fig. 2, the wave vector has also been rescaled accordingly. Therefore Figs. 2 and 3 can be compared directly. Obviously, in the homogeneous gauge, significant degeneracies on a 60×60 lattice exist, which lead to rather large discretization effects [e.g., Fig. 3(a)]. Therefore spectra for the homogeneous gauge in Fig. 3 are displayed employing an imaginary broadening $O(10)$ times larger than for the random gauge configuration, where averaging leads to almost "self-smoothed" spectra. We note that for the random gauge, 60×60 lattices imply diagonalizations of dense 7200×7200 matrices, which is still just within acceptable reach of standard libraries.

Several features can be observed. First, while the ph channel in the uniform gauge definitely displays the singular behavior at $\omega = \epsilon_{\tilde{\mathbf{q}}}$, mentioned earlier and clearly visible because of the higher temperatures, in the random gauge case, it displays just a smooth peak. Second, as can be read off the y axis, the weight of the ph channel strongly increases with

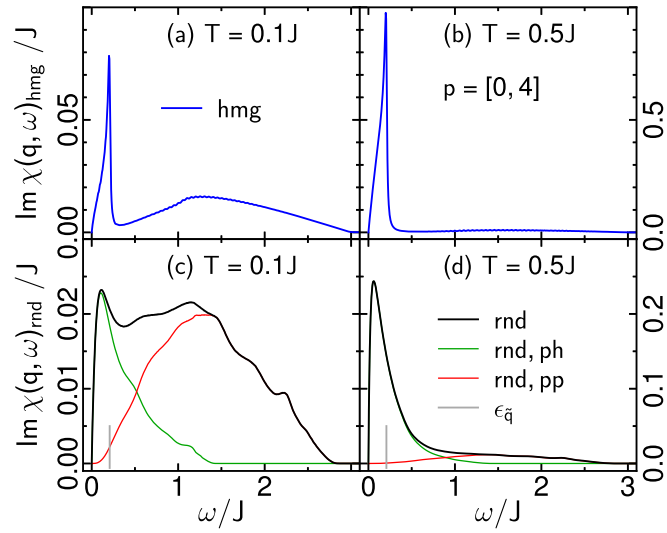

FIG. 3. Spectrum, $\mathrm{Im}\chi(\mathbf{q}, \omega)$, of the energy-density susceptibility vs ω at fixed small $\mathbf{q}$ set by p, contrasting the homogeneous gauge [(a) and (b), blue] with the random (rnd) gauge [(c) and (d), black] for two temperatures, $T = 0.1J$ [(a) and (c)] and $T = 0.5J$ [(b) and (d)]. For the random gauge, the ph (green), and pp spectra (red) are also displayed. All system sizes are $L^2 = 60 \times 60$. The vertical gray line in (c) and (d) shows the upper ph-continuum bound at $\mathbf{q}$. Imaginary broadening in the homogeneous gauge [(a) and (b)] is chosen to leave singular behavior of the ph-continuum visible.

increasing T. For the temperatures depicted, the pp channel is much less T dependent. Third, the ph and pp contributions to $\mathrm{Im}\chi(\mathbf{q}, \omega)$ not only can be separated in the uniform gauge configuration by virtue of Eqs. (6) but also can be separated in the random gauge configuration, i.e., Eq. (9) can be decomposed into addends with $\epsilon_\sigma \epsilon_\rho \gtrless 0$. This evidences that in the latter case, the ph spectrum changes completely. As is obvious from Figs. 3(c) and 3(d), the ph channel spreads into a broad feature, extending over roughly the entire one-particle energy range. The pp channel, on the other hand, seems less affected by the random gauge, with a shape qualitatively similar to that in the homogeneous gauge. This can be read off by comparing, e.g., Figs. 3(a) and 3(c).

Most remarkably, for intermediate temperatures, as in Fig. 3(d) at $T = 0.5J$, the overall shape of the spectrum is very reminiscent of a diffusion-pole behavior at fixed momentum, i.e., $\mathrm{Im}\chi(\mathbf{q}, \omega) \propto \omega\Gamma/(\omega^2 + \Gamma^2)$, with some relaxation rate Γ.

1. Hydrodynamic description

To put the preceding findings into perspective, we proceed and analyze $\chi(\mathbf{q}, \omega)$ in terms of the hydrodynamic expression (10). To this end, we first extract the static susceptibility $\chi_{\mathbf{q}}$, performing the sum rule of Eq. (11) via numerical integration, using $\mathrm{Im}\chi(\mathbf{q}, \omega)$ from random gauge configuration averages. Typical results are shown in Fig. 4, comprising a complete irreducible $\boldsymbol{q}$ wedge of the BZ for $L^2 = 30 \times 30$ and selected momenta for $L^2 = 60 \times 60$. As is obvious, the finite-size effects are small. Since energy conservation renders the dynamical density response singular at $\boldsymbol{q} = \mathbf{0}$, this momentum

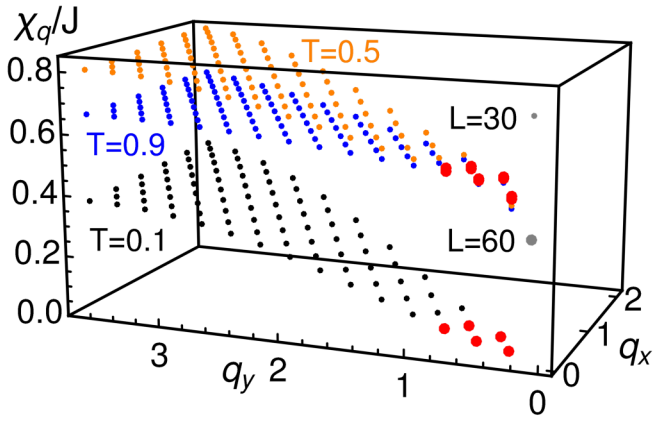

FIG. 4. Static susceptibility χ_q vs momentum in the random gauge configuration on a complete irreducible wedge of BZ at $L^2 = 30 \times 30$ (small solid dots) for three temperatures $T/J = 0.1, 0.5$, and 0.9 (black, orange, and blue). Big solid red dots show the results on $L^2 = 60 \times 60$ at selected $\boldsymbol{q}$ also $\in 30 \times 30$ BZ.

will be excluded hereafter. The main message of this figure is that $\chi_{\mathbf{q}}$ is a smooth and featureless function.

Next, we consider the global variation with momentum of the spectrum of the *normalized* dynamical energy-density susceptibility [Figs. 5(a) and 5(b)] and that of the diffusion kernel [Figs. 5(c) and 5(d)], versus ω. Two temperatures, i.e., $T/J = 0.1$ and 0.5, are chosen in Figs. 5(a) and 5(c), and Figs. 5(b) and 5(d), respectively. Since our focus is on the hydrodynamic regime, we consider five small momenta $\mathbf{q}_{i=1\cdots5}$. These momenta are indicated on a fraction of an irreducible wedge of the BZ in Fig. 5(b). Their integer doublets are listed in Fig. 5(d). A spacing of mod(2) of the momenta has been chosen to allow for later analysis of finite-size effects in comparison to systems with a linear dimension that is smaller by a factor of 2; see Appendix A. While Fig. 5 covers temperatures

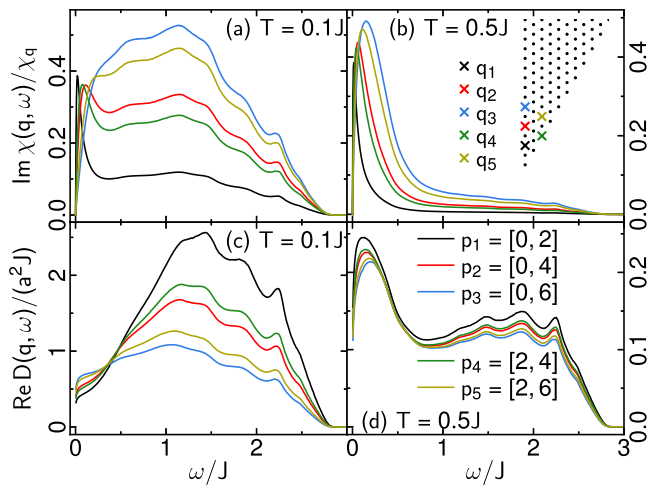

FIG. 5. Imaginary part of the normalized density susceptibility $\bar{\chi}(\mathbf{q}, \omega)$ [(a) and (b)] and real part of diffusion kernel $\mathrm{Re}D(\mathbf{q}, \omega)$ [(c) and (d)] in the random gauge, at two temperatures, $T/J = 0.1$ [(a) and (c)] and $T/J = 0.5$ [(b) and (d)], vs ω, for five momenta $\mathbf{q}_{i=1\cdots5}$, set by p_i, and displayed on part of the BZ wedge. System size is $L^2 = 60 \times 60$. In (c) and (d), $\omega \geqslant 0.005J$; see Sec. IV B 1.

up to intermediate values of $T = 0.5J$, we find that above this range, the quantities depicted acquire only little additional change, as compared with $T = 0.5T$. For completeness, we present such results in Appendix B.

There is a clear difference between the spectra of $\bar{\chi}(\mathbf{q}, \omega)$ at low and intermediate temperatures, i.e., Figs. 5(a) and 5(b). Both display a broadening of their intensity representing the ph channel and an increase in weight within the range of the pp excitations as $|\boldsymbol{q}|$ increases. However, the relative dominance of these two effects is reversed as the temperature increases from 0.1 to $0.5J$. This is a direct consequence of the rapid increase in the Fermi volume as T increases.

The real part of the corresponding diffusion kernel $D(\mathbf{q}, \omega)$, is depicted in Figs. 5(c) and 5(d). Clearly, at low T, i.e., Fig. 5(c), the diffusion kernel displays significant variation with $\boldsymbol{q}$. This implies that density modes at fixed $\mathbf{q}$ do not relax in proportion to q^2 only, and therefore a simple hydrodynamic picture is not applicable. That is, q^2 scaling, as defined in Sec. III C, does not hold. In contrast to that, at intermediate T, i.e., Fig. 5(d), the diffusion kernel is almost momentum independent, i.e., $\mathrm{Re}D(|\mathbf{q}| \ll 1, \omega) \simeq \mathrm{Re}D(\omega)$. In fact, while q^2 differs by a factor of 9 between, e.g., p_1 and p_3, $\mathrm{Re}D(\mathbf{q}, \omega)$ differs by only $\sim$20% between the two momenta. This is approximately consistent with Fick's law regarding $\boldsymbol{q}$ scaling. This property persists above this temperature, as shown in Appendix B.

Regarding the energy, however, the diffusion kernel remains retarded, i.e., $D(\mathbf{q}, \omega)$ is not constant versus ω. Speaking differently, any density mode at a given momentum $\mathbf{q}$ will not decay with a plain exponential in time. First, as $\omega/J \to 0$, the diffusion kernel exhibits a very narrow dip, i.e., a reduction in its amplitude for $\omega/J \lesssim 0.1$. As $\omega/J \to 0$, the numerical accuracy of the transform equation (12), comprising small numbers in the numerator and denominator, is an issue with respect to system size and imaginary broadening. Therefore we have to remain with $\omega \geqslant \omega_{\min} = 0.005J$ for the diffusion kernel, as indicated in the caption of Fig. 5. See also the discussion of Fig. 8 in Appendix A. In view of the steep slope in this regime, the limiting value of $\mathrm{Re}D(|\mathbf{q}| \ll 1, \omega = 0)$ on our finite systems is an open issue. Suggesting a singularly vanishing diffusion kernel at $\omega = 0$ from Figs. 5(c) and 5(d) may be tempting; however, this would imply an insulator regarding energy transport. Interestingly, exactly the latter question has already been considered in the literature [63], where extensive finite-size analysis of a similar low-ω structure has proven that the energy *conductivity* remains finite. In turn, in the thermodynamic limit of $\mathrm{Re}D(|\mathbf{q}| \ll 1, \omega = 0)$ it will remain finite and likely of the order of the low-energy peak height. To substantiate this claim, we will relate our findings to those of the known energy conductivity in Sec. IV B 2.

The remaining energy dependence, once again, relates to the two relaxation channels, i.e., a broad peak from ph excitations followed by a flat shoulder from pp excitations. On top of this flat shoulder, and at the upper part of its energy range, some additional "wiggles" can be observed, which are also visible in $\bar{\chi}(\mathbf{q}, \omega)$, yet less pronounced. These wiggles are no numerical artifact or finite-size effect. They stem from known modulations of the density of states rooted in the scattering of the fermions from the potentials of the excited static fluxes

[61,71]. For $\omega/J \gtrsim 2.8$, the spectral support terminates, and the diffusion kernel turns purely imaginary $\propto \omega^{-1}$. The reduction of the bandwidth to less than $3J$ is an effect of the gauge fluctuations.

In conclusion, at not-too-low temperatures and not-too-short time scales, random gauge configurations in the Kitaev magnet lead to an energy-density dynamics, very similar to conventional diffusion, regarding its momentum scaling, with, however, some retardation remaining. This should be contrasted with the underlying spin model being a translationally invariant system.

2. Current correlation function

In the limit of $\boldsymbol{q} \to \mathbf{0}$ one may ask whether the dynamical energy-density diffusion kernel is connected to the dynamical energy-current correlation function via a generalized Einstein relation. The zero-momentum current correlation function has been considered in Ref. [63]. For the sake of completeness, we now clarify how to relate the latter quantity to the present work. This serves two purposes. First, it shows that a remarkable consistency exists between the present work and other calculations of a different correlation function. Second, it provides additional insight into the dip at very low ω of the diffusion kernel. From Mori-Zwanzig's projection method [73] we have

$$\frac{1}{\omega}[\chi_{\mathbf{q}} - \chi(\mathbf{q},\omega)] = \frac{1}{\omega - M(\mathbf{q},\omega)\frac{1}{\chi_{\mathbf{q}}}}\chi_{\mathbf{q}}, \tag{13}$$

where $M(\mathbf{q},\omega) = \langle Lh_{\mathbf{q}}|(\omega - QL)^{-1}QLh_{\mathbf{q}}\rangle$ is the memory function. L is the Liouville operator $LA = [H, A]$, and $\langle A|B\rangle = \int_0^\beta \langle A^+(\lambda)B\rangle d\lambda - \beta\langle A^+\rangle\langle B\rangle$ is Mori's scalar product, where $A(\lambda) = e^{\lambda H}Ae^{-\lambda H} = e^{\lambda L}A$ and $\beta = 1/T$ is the inverse temperature. $\chi_{\mathbf{q}}$ is the isothermal energy susceptibility $\chi_{\mathbf{q}} = \langle h_{\mathbf{q}}|h_{\mathbf{q}}\rangle$, and Q is a projector perpendicular to the energy density, which is formulated using Mori's product as $Q = 1 - |h_{\mathbf{q}}\rangle\chi_{\mathbf{q}}^{-1}\langle h_{\mathbf{q}}|$. We emphasize that Eq. (13) is *not* a "high-frequency," or "slow-mode," approximation. It is a rigorous statement. Due to time-reversal invariance, $QLh_{\mathbf{q}} = Lh_{\mathbf{q}}$ [73]. Moreover, using the continuity equation in the hydrodynamic regime, i.e., discarding the lattice structure, we have $Lh_{\mathbf{q}} = -\mathbf{q}\cdot\mathbf{j}_{\mathbf{q}}$, where $\mathbf{j}_{\mathbf{q}}$ is the energy current. Altogether,

$$i\chi_{\mathbf{q}}D(\mathbf{q},\omega) = \sum_{\mu\nu} e_{q\mu}e_{q\nu}\left\langle j_{q\mu}\left|\frac{1}{\omega - QL}j_{q\nu}\right.\right\rangle, \tag{14}$$

where $\boldsymbol{e}_{q\mu}$ are the components of the unit vector in the $\boldsymbol{q}$ direction. While for arbitrary $\boldsymbol{q}$ the right-hand side refers to a so-called current relaxation function with a dynamics governed by a projected Liouville operator QL, for $\boldsymbol{q} \to \mathbf{0}$ one finds that $\lim_{q\to\mathbf{0}}\langle j_{q\mu}|(\omega - QL)^{-1}j_{q\nu}\rangle = \langle j_{\mathbf{0}\mu}|(\omega - L)^{-1}j_{\mathbf{0}\nu}\rangle$ [73], which is the genuine current relaxation function comprising the complete Liouvillean dynamics. This turns Eq. (14) into an Einstein relation for $\boldsymbol{q} \to \mathbf{0}$. Finally, the spectrum of the current relaxation function can be related to that of a standard current correlation function $C_{\mu\nu}(t) = \langle j_{\mathbf{0}\mu}(t)j_{\mathbf{0}\nu}\rangle$ by the Kubo relation and the fluctuation dissipation theorem

$$C(\mathbf{q},\omega) = \frac{2\omega}{1 - e^{\omega/T}}\chi_{\mathbf{q}}\,\mathrm{Re}D(\mathbf{q},\omega), \tag{15}$$

$$C(\omega) = \lim_{\boldsymbol{q}\to\mathbf{0}} C(\mathbf{q},\omega). \tag{16}$$

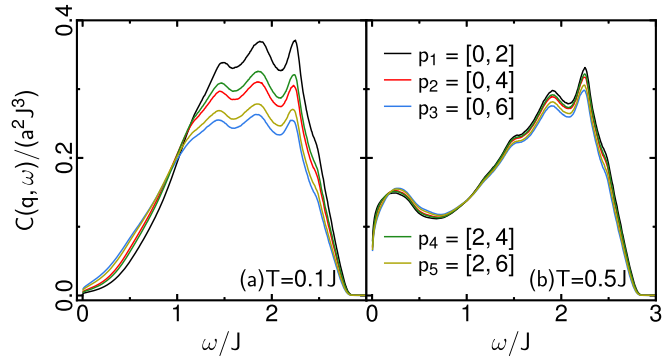

FIG. 6. Current correlation function $C(\mathbf{q},\omega)$ in the random gauge, at two temperatures, $T = 0.1J$ (a) and $0.5J$ (b), vs $\omega \geqslant 0.005J$, for five momenta $\mathbf{q}_{i=1\cdots5}$, identical to Fig. 5(b), set by p_i. System size is $L^2 = 60 \times 60$.

Here, we have discarded questions of anisotropy. While the focus of this paper is on $\boldsymbol{q} \neq 0$, it is now very tempting to evaluate the left-hand side of Eq. (15) using, e.g., the two temperatures of Figs. 5(c) and 5(d) and to consider its evolution with the momenta displayed therein. This is shown in Fig. 6. This figure should be compared with Figs. 5(b) and 5(d) of Ref. [63]. For this, and because of a different energy unit and normalization of spectral densities in the latter reference, T has to rescaled by 4, and the y axis has to be rescaled by $4^3/\pi$. While the rescaled temperatures $T = 0.025$ and 0.525 of Ref. [63] are not completely identical to the ones we use, it is very satisfying to realize that the limit $\boldsymbol{q} \to \mathbf{0}$ of Eq. (16), which can be anticipated from Figs. 6(a) and 6(b), is completely in line with Figs. 5(b) and 5(d) of Ref. [63]. This includes the dip at very low ω. This is even more remarkable in view of the numerical representation and treatment of the Majorana fermions used in this paper and in Ref. [63] being decisively different.

Apart from these considerations being a consistency check on the present work, we can now rely on the extensive finite-size analysis performed in Ref. [63] to suggest that in the thermodynamic limit the narrow dip will eventually leave $\mathrm{Re}D(|\mathbf{q}| \ll 1, \omega = 0)$ finite and of the order of the low-energy peak height.

3. Temperature dependence

Turning to the temperature dependence of the diffusion kernel, we consider two representative momenta $\boldsymbol{q}$ and several energies. The corresponding diffusion kernel $\mathrm{Re}D(\mathbf{q},\omega)$ and the static susceptibility $\chi_{\boldsymbol{q}}$ are shown versus T in Figs. 7(a) and 7(b) and Figs. 7(c) and 7(d), respectively. The temperature range has been restricted to $T \gtrsim 0.25J$. The latter is motivated by the discussion of Figs. 5(c) and 5(d). There we showed that while for $T = 0.1J \gg T^\star$ the gauge is clearly in its random configuration, the Fermi volume is not yet large enough to allow for a diffusion process with hydrodynamic q^2 scaling.

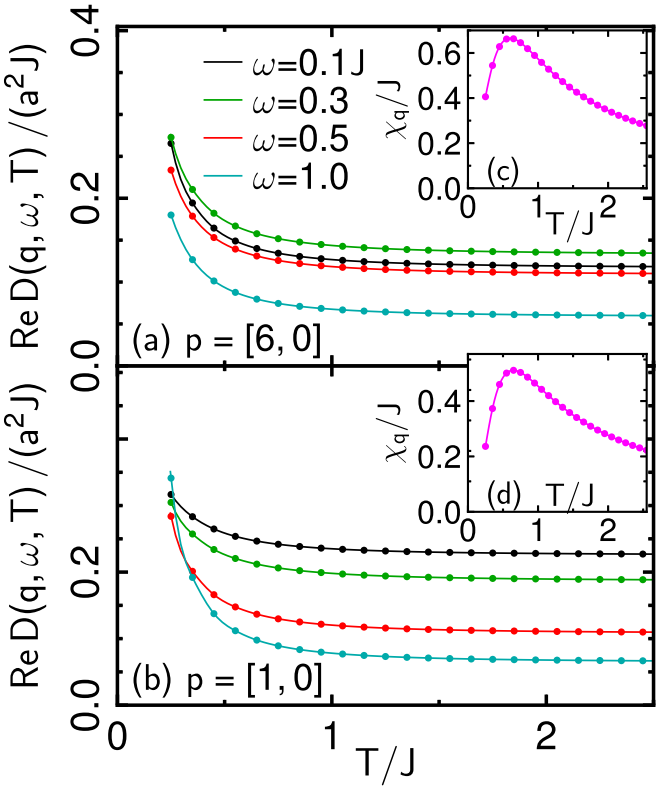

FIG. 7. Real part of the diffusion kernel Re$D(\mathbf{q}, \omega, T)$ [(a) and (b)], for four energies $\omega/J = 0.1 \cdots 1.0$, and static susceptibility $\chi_{\boldsymbol{q}}(T)$ [(c) and (d)], in the random gauge vs T, for two momenta, set by $p = [6, 0]$ [(a) and (c)] and [1,0] [(b) and (d)]. System size is $L^2 = 30 \times 30$.

At $T = 0.5J$, however, we observe approximate q^2 scaling. Therefore we start the analysis at a temperature roughly in between. Figures 7(a) and 7(b) clearly demonstrate, that for $T \gtrsim 0.5J$, the diffusion kernel rapidly settles onto some almost constant value, set by energy and momentum. This can also be seen by comparing Fig. 5(d) with Fig. 9(b) in Appendix B. These figures evidence only weak overall change between the diffusion kernels for intermediate and elevated temperatures. As a consequence, the global T dependence of $\chi(\boldsymbol{q}, \omega)$ for $T \gtrsim 0.5J$ is essentially set by the static energy susceptibility. As Figs. 7(c) and 7(d) show, the latter exhibits a maximum roughly at the start of this temperature range. For $T/J \gg 1$, $\chi_{\mathbf{q}}$ approaches its high-temperature classical limit, decaying $\propto T^{-1}$, which can also be read off from the high-temperature expansion of the Fermi functions of Eqs. (11) and (9). Such behavior is typical also for other static susceptibilities of spin systems at high temperatures.

V. DISCUSSION

To recapitulate, we have studied the energy dynamics of the Kitaev model on a honeycomb lattice. Exchange frustration [see Fig. 1 and Eq. (1)] induces a fractionalization of spin operators into a $\mathbb{Z}_2$ gauge field and itinerant Majorana fermions [Eq. (2)]. This leads to a very interesting energy dynamics with three distinct temperature regimes. At very low temperatures $T \lesssim T^*$, the gauge field is frozen into a homogeneous configuration, and therefore the itinerant fermions transfer energy in a uniform medium, in a ballistic way. At somewhat higher, yet still rather low temperatures, in a range of approximately $T^* \lesssim T/J \lesssim 0.1$, the thermal population of random gauge field configurations forces the fermions to move in a disordered environment, despite the fact that the model in the spin representation is translationally invariant. The energy dynamics in this regime ceases to be ballistic but is also not diffusive. This is manifest through, for example, the strong q dependence of the diffusion kernel [Fig. 5(c)]. We attribute this behavior to the restricted phase space at the bottom of the Dirac cone, distorted by gauge flips. Finally, starting at intermediate temperatures, $T \gtrsim 0.5J$, which is still well below the high-temperature classical limit, $T \gg J$, the relaxation of the energy density in Kitaev magnets at finite momentum is remarkably similar to diffusion in random media, with, however, a clearly notable difference. On the one hand, the relaxation practically displays a hydrodynamic q^2 scaling, with a diffusion kernel that is almost momentum independent. On the other hand, the diffusion kernel is not completely frequency independent, i.e., it displays some retardation within its support. The origin of the latter can be traced back to the presence of two distinct relaxation channels for the energy density, comprising particle-hole and particle-particle excitations of the Dirac fermions. Their combination does not lead to a constant diffusion rate of the energy versus frequency at fixed momentum. The physical significance of this is that any density mode at given momentum $\mathbf{q}$ will not decay with a plain exponential in time.

Another interesting observation arises at extremely low energies, $\omega/J \to 0$, in Fig. 5, where we observe a depletion of the diffusion kernel in a very narrow ω range. This is consistent with a similar behavior of the dynamical thermal conductivity [62,63,70], to which we find that our results connect consistently via generalized Einstein relations. This low-frequency dip at $D(\mathbf{q}, \omega)$ is one more indication of the reduction in energy transport by the fermions due to the thermally induced disorder caused by the gauge field fluctuations. Interpreting the low-energy dip as one contribution to the retardation, it implies a slowing down of the density relaxation at long times scales.

From a more general perspective, the very details described in this paper are certainly specific to the Kitaev model, including the particular gauge field with no dynamics and an exponentially large number of conserved flux configurations. While this also relates to the integrability of the model, the main point rather is that the majority of gauge sectors break translational invariance. The latter is not specific to the Kitaev model only, and connects to the broader physics of internal "randomness," self-localization, and questions of ergodicity, induced by superselection sectors in *a priori* translationally invariant models of gauge theories, which is of current interest in various other systems [65–67] and in the context many-body localization [68].

Future analysis, focusing not only on the hydrodynamic regime but also on wave vectors close to the high-symmetry points of the Brillouin zone, could further improve understanding of the energy dynamics in such spin liquids. In particular, studying the real-space dependence, instead of the momentum-space dependence, of the energy-density

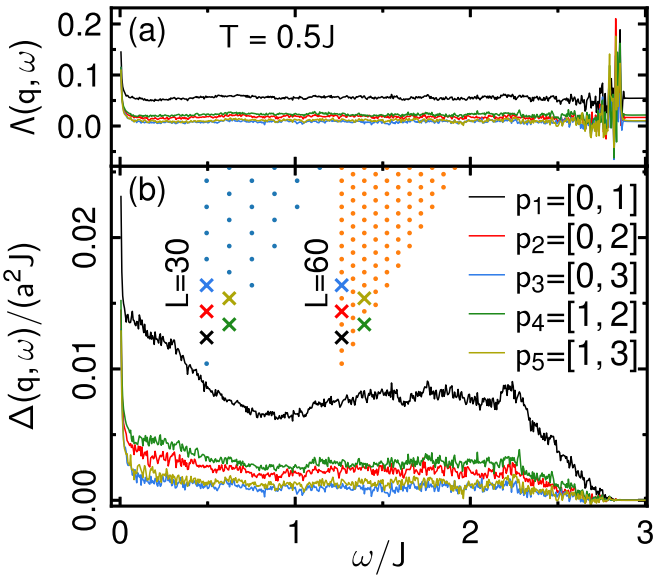

FIG. 8. Relative (a) and absolute (b) difference, $\Lambda(\mathbf{q},\omega)$ and $\Delta(\mathbf{q},\omega)$, respectively, of the real part of the diffusion kernel at $T = 0.5J$, between a $L^2 = 30\times 30$ and a $L^2 = 60\times 60$ system, in the random gauge, vs $\omega \geqslant 0.005J$, at five momenta $\mathbf{q}_{i=1\cdots5}$, displayed on parts of the respective BZ wedge and set by $p_i(2p_i)$ for $L^2 = 30\times 30$ (60×60).

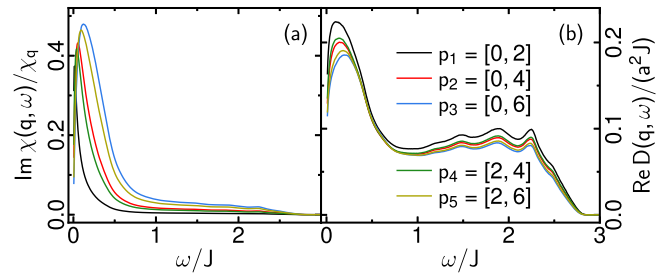

FIG. 9. Imaginary part of the normalized density susceptibility $\bar{\chi}(\mathbf{q},\omega)$ (a) and real part of diffusion kernel $\mathrm{Re}D(\mathbf{q},\omega)$ (b) in the random gauge, at an elevated temperature $T = 0.9J$, vs ω, for five momenta $\mathbf{q}_{i=1\cdots5}$ shown in Fig. 5(b) and set by p_i. System size is $L^2 = 60\times 60$. In (b), $\omega \geqslant 0.005J$; see Sec. IV B 1.

relaxation could be interesting in order to predict finite-temperature quench dynamics, as, e.g., in pump-probe experiments.

ACKNOWLEDGMENTS

This work has been supported in part by the DFG through Project A02 of SFB 1143 (Project No. 247310070), by Niedersächsisches Vorab QUANOMET (Project NP-2), and by the National Science Foundation under Grant No. NSF PHY-1748958. W.B. also acknowledges the kind hospitality of the PSM, Dresden.

APPENDIX A: NUMERICAL ACCURACY

Here, we provide some rough measure of the numerical errors from the random realizations, finite-size effects, and sum-rule transforms involved in our calculations. To this end, we consider both the absolute and the relative difference between the real parts of the diffusion kernels, $\Delta(\mathbf{q},\omega) = |\mathrm{Re}[D_{30\times30}(\mathbf{q},\omega) - D_{60\times60}(\mathbf{q},\omega)]|$ and $\Lambda(\mathbf{q},\omega) = 2\Delta(\mathbf{q},\omega)/|\mathrm{Re}[D_{30\times30}(\mathbf{q},\omega) + D_{60\times60}(\mathbf{q},\omega)]|$, on $N = 30\times30$-site and $N = 60\times60$-site systems, respectively, for identical wave vectors.

Regarding the wave vectors, this requires a factor of 2 difference between their integer representations p in terms of the reciprocal lattice vectors $\mathbf{G}_{1,2}$. This divisibility by 2 has been taken into account in our calculations on $N = 60\times60$-site systems, as can be seen in the caption of Figs. 5(b) and 5(d).

$\Lambda(\mathbf{q},\omega)$ and $\Delta(\mathbf{q},\omega)$ are shown in Figs. 8(a) and 8(b). They display very low statistical noise from the finite number of 200 random gauge realizations employed throughout this paper, justifying the use of this number. The increase in $\Lambda(\mathbf{q},\omega)$ at the upper edge of the spectrum is due only to its definition, comprising a division by a very small number in this regime.

Except for very small ω and the aforementioned upper spectral edge, the relative finite-size errors, $\Lambda(\mathbf{q},\omega)$, are less than $\sim$6%. As is to be expected, this error is largest for the smallest wave vector and is actually even less than $\sim$3% for all remaining wave vectors.

Finally, for $\omega \ll 0.01$, where $\Lambda(\mathbf{q},\omega)$ is $O(10\%)$, the error is not of finite size, or statistical origin, but stems from the systematic numerical inaccuracies, mentioned in Sec. IV B 1, and is generated by the denominator in Eq. (12) with $\chi(\mathbf{q},\omega)$ obtained from Eq. (9) as $\omega \to 0$. In turn, $D(\mathbf{q},\omega)$ at very low $\omega \ll 0.01$ may be inaccurate by $\sim$10%. This explains why we have remained with $\omega \geqslant 0.005J$ in figures displaying results related to the diffusion kernel versus ω.

APPENDIX B: ELEVATED TEMPERATURE, $T > 0.5J$

For the sake of completeness, in this Appendix, i.e., in Fig. 9, we show additional results for the normalized dynamical susceptibility and the diffusion kernel, similar to Fig. 5, at a rather elevated temperature $T = 0.9J$, which, however, is still well below the high-temperature classical limit, as discussed with respect to Fig. 7. As is obvious, there is neither a qualitative nor a significant quantitative difference between results at $T = 0.5J$ [Figs. 5(b) and 5(d)] and results at $T = 0.9J$ [Figs. 9(a) and 9(b)]. This is completely consistent with the discussion of Fig. 7, where it was shown that above $T \gtrsim 0.5J$ the temperature dependence is essentially encapsulated in $\chi_{\mathbf{q}}$.

[1] A. V. Sologubenko, E. Felder, K. Giannò, H. R. Ott, A. Vietkine, and A. Revcolevschi, Phys. Rev. B **62**, R6108(R) (2000).

[2] T. Kawamata, N. Takahashi, T. Adachi, T. Noji, K. Kudo, N. Kobayashi, and Y. Koike, J. Phys. Soc. Jpn. **77**, 034607 (2008).

[3] N. Hlubek, P. Ribeiro, R. Saint-Martin, A. Revcolevschi, G. Roth, G. Behr, B. Büchner, and C. Hess, Phys. Rev. B **81**, 020405(R) (2010).

[4] A. V. Sologubenko, K. Giannò, H. R. Ott, U. Ammerahl, and A. Revcolevschi, Phys. Rev. Lett. **84**, 2714 (2000).

[5] C. Hess, C. Baumann, U. Ammerahl, B. Büchner, F. Heidrich-Meisner, W. Brenig, and A. Revcolevschi, Phys. Rev. B **64**, 184305 (2001).

[6] X. Zotos, F. Naef, and P. Prelovsek, Phys. Rev. B **55**, 11029 (1997).

[7] F. Heidrich-Meisner, A. Honecker, D. C. Cabra, and W. Brenig, Phys. Rev. B **68**, 134436 (2003).

[8] F. Heidrich-Meisner, A. Honecker, D. C. Cabra, and W. Brenig, Phys. Rev. Lett. **92**, 069703 (2004).

[9] C. Hess, Eur. Phys. J.: Spec. Top. **151**, 73 (2007).

[10] F. Heidrich-Meisner, A. Honecker, and W. Brenig, Eur. Phys. J.: Spec. Top. **151**, 135 (2007).

[11] C. Hess, Phys. Rep. **811**, 1 (2019).

[12] B. Bertini, F. Heidrich-Meisner, C. Karrasch, T. Prosen, R. Steinigeweg, and M. Žnidarič, Rev. Mod. Phys. **93**, 025003 (2021).

[13] A. Kitaev, Ann. Phys. (Amsterdam) **321**, 2 (2006).

[14] J. Wang, Y. K. Takahashi, and K.-i. Uchida, Nat. Commun. **11**, 2 (2020).

[15] S. R. Boona, R. C. Myers, and J. P. Heremans, Energy Environ. Sci. **7**, 885 (2014).

[16] N. Terakado, Y. Nara, Y. Machida, Y. Takahashi, and T. Fujiwara, Sci. Rep. **10**, 14468 (2020).

[17] M. Otter, G. Athanasopoulos, N. Hlubek, M. Montagnese, M. Labois, D. A. Fishman, F. de Haan, S. Singh, D. Lakehal, J. Giapintzakis, C. Hess, A. Revcolevschi, and P. H. M. van Loosdrecht, Int. J. Heat Mass Transfer **55**, 2531 (2012).

[18] G. S. Dixon, Phys. Rev. B **21**, 2851 (1980).

[19] C. Hess, B. Büchner, U. Ammerahl, L. Colonescu, F. Heidrich-Meisner, W. Brenig, and A. Revcolevschi, Phys. Rev. Lett. **90**, 197002 (2003).

[20] S. P. Bayrakci, B. Keimer, and D. A. Tennant, arXiv:1302.6476 [cond-mat.str-el].

[21] A. L. Chernyshev and W. Brenig, Phys. Rev. B **92**, 054409 (2015).

[22] L. Balents, Nature (London) **464**, 199 (2010).

[23] L. Savary and L. Balents, Rep. Prog. Phys. **80**, 016502 (2017).

[24] M. Yamashita, N. Nakata, Y. Senshu, M. Nagata, H. M. Yamamoto, R. Kato, T. Shibauchi, and Y. Matsuda, Science **328**, 1246 (2010).

[25] P. Bourgeois-Hope, F. Laliberté, E. Lefrançois, G. Grissonnanche, S. R. de Cotret, R. Gordon, S. Kitou, H. Sawa, H. Cui, R. Kato, L. Taillefer, and N. Doiron-Leyraud, Phys. Rev. X **9**, 041051 (2019).

[26] J. M. Ni, B. L. Pan, B. Q. Song, Y. Y. Huang, J. Y. Zeng, Y. J. Yu, E. J. Cheng, L. S. Wang, D. Z. Dai, R. Kato, and S. Y. Li, Phys. Rev. Lett. **123**, 247204 (2019).

[27] G. Kolland, O. Breunig, M. Valldor, M. Hiertz, J. Frielingsdorf, and T. Lorenz, Phys. Rev. B **86**, 060402(R) (2012).

[28] W. H. Toews, S. S. Zhang, K. A. Ross, H. A. Dabkowska, B. D. Gaulin, and R. W. Hill, Phys. Rev. Lett. **110**, 217209 (2013).

[29] Y. Tokiwa, T. Yamashita, D. Terazawa, K. Kimura, Y. Kasahara, T. Onishi, Y. Kato, M. Halim, P. Gegenwart, T. Shibauchi, S. Nakatsuji, E.-G. Moon, and Y. Matsuda, J. Phys. Soc. Jpn. **87**, 064702 (2018).

[30] M. Hirschberger, R. Chisnell, Y. S. Lee, and N. P. Ong, Phys. Rev. Lett. **115**, 106603 (2015).

[31] D. Watanabe, K. Sugii, M. Shimozawa, Y. Suzuki, T. Yajima, H. Ishikawa, Z. Hiroi, T. Shibauchi, Y. Matsuda, and M. Yamashita, Proc. Natl. Acad. Sci. USA **113**, 8653 (2016).

[32] M. Yamashita, M. Akazawa, M. Shimozawa, T. Shibauchi, Y. Matsuda, H. Ishikawa, T. Yajima, Z. Hiroi, M. Oda, H. Yoshida, H.-Y. Lee, J. H. Han, and N. Kawashima, J. Phys.: Condens. Matter **32**, 074001 (2019).

[33] M. Hirschberger, J. W. Krizan, R. J. Cava, and N. P. Ong, Science **348**, 106 (2015).

[34] X.-Y. Feng, G.-M. Zhang, and T. Xiang, Phys. Rev. Lett. **98**, 087204 (2007).

[35] H.-D. Chen and Z. Nussinov, J. Phys. A: Math. Theor. **41**, 075001 (2008).

[36] Z. Nussinov and G. Ortiz, Phys. Rev. B **79**, 214440 (2009).

[37] S. Mandal, R. Shankar, and G. Baskaran, J. Phys. A: Math. Theor. **45**, 335304 (2012).

[38] S. Trebst, Kitaev materials, in *Topological Matter - Topological Insulators, Skyrmions and Majoranas, Lecture Notes of the 48th IFF Spring School 2017*, edited by S. Blügel, Y. Mokrousov, T. Schäpers, and Y. Ando (Forschungszentrum Jülich, Jülich, Germany, 2017), Chap. D3, pp. 769–807.

[39] K. W. Plumb, J. P. Clancy, L. J. Sandilands, V. V. Shankar, Y. F. Hu, K. S. Burch, H.-Y. Kee, and Y.-J. Kim, Phys. Rev. B **90**, 041112(R) (2014).

[40] A. Banerjee, C. A. Bridges, J. Q. Yan, A. A. Aczel, L. Li, M. B. Stone, G. E. Granroth, M. D. Lumsden, Y. Yiu, J. Knolle, S. Bhattacharjee, D. L. Kovrizhin, R. Moessner, D. A. Tennant, D. G. Mandrus, and S. E. Nagler, Nat. Mater. **15**, 733 (2016).

[41] A. Banerjee, J. Yan, J. Knolle, C. A. Bridges, M. B. Stone, M. D. Lumsden, D. G. Mandrus, D. A. Tennant, R. Moessner, and S. E. Nagler, Science **356**, 1055 (2017).

[42] A. Banerjee, P. Lampen-Kelley, J. Knolle, C. Balz, A. A. Aczel, B. Winn, Y. Liu, D. Pajerowski, J. Yan, C. A. Bridges, A. T. Savici, B. C. Chakoumakos, M. D. Lumsden, D. A. Tennant, R. Moessner, D. G. Mandrus, and S. E. Nagler, npj Quantum Mater. **3**, 8 (2018).

[43] J. Knolle, G. W. Chern, D. L. Kovrizhin, R. Moessner, and N. B. Perkins, Phys. Rev. Lett. **113**, 187201 (2014).

[44] D. Wulferding, Y. Choi, S.-H. Do, C. H. Lee, P. Lemmens, C. Faugeras, Y. Gallais, and K.-Y. Choi, Nat. Commun. **11**, 1603 (2020).

[45] S.-H. Baek, S.-H. Do, K. Y. Choi, Y. S. Kwon, A. U. B. Wolter, S. Nishimoto, J. van den Brink, and B. Büchner, Phys. Rev. Lett. **119**, 037201 (2017).

[46] J. Zheng, K. Ran, T. Li, J. Wang, P. Wang, B. Liu, Z.-X. Liu, B. Normand, J. Wen, and W. Yu, Phys. Rev. Lett. **119**, 227208 (2017).

[47] D. Hirobe, M. Sato, Y. Shiomi, H. Tanaka, and E. Saitoh, Phys. Rev. B **95**, 241112(R) (2017).

[48] I. A. Leahy, C. A. Pocs, P. E. Siegfried, D. Graf, S.-H. Do, K.-Y. Choi, B. Normand, and M. Lee, Phys. Rev. Lett. **118**, 187203 (2017).

[49] R. Hentrich, A. U. B. Wolter, X. Zotos, W. Brenig, D. Nowak, A. Isaeva, T. Doert, A. Banerjee, P. Lampen-Kelley, D. G. Mandrus, S. E. Nagler, J. Sears, Y.-J. Kim, B. Büchner, and C. Hess, Phys. Rev. Lett. **120**, 117204 (2018).

[50] Y. J. Yu, Y. Xu, K. J. Ran, J. M. Ni, Y. Y. Huang, J. H. Wang, J. S. Wen, and S. Y. Li, Phys. Rev. Lett. **120**, 067202 (2018).

[51] Y. Kasahara, T. Ohnishi, Y. Mizukami, O. Tanaka, S. Ma, K. Sugii, N. Kurita, H. Tanaka, J. Nasu, Y. Motome, T. Shibauchi, and Y. Matsuda, Nature (London) **559**, 227 (2018).
[52] T. Yokoi, S. Ma, Y. Kasahara, S. Kasahara, T. Shibauchi, N. Kurita, H. Tanaka, J. Nasu, Y. Motome, C. Hickey, S. Trebst, and Y. Matsuda, Science **373**, 568 (2021).
[53] G. Baskaran, S. Mandal, and R. Shankar, Phys. Rev. Lett. **98**, 247201 (2007).
[54] J. Knolle, D. L. Kovrizhin, J. T. Chalker, and R. Moessner, Phys. Rev. Lett. **112**, 207203 (2014).
[55] J. Nasu, J. Knolle, D. L. Kovrizhin, Y. Motome, and R. Moessner, Nat. Phys. **12**, 912 (2016).
[56] G. B. Halász, N. B. Perkins, and J. van den Brink, Phys. Rev. Lett. **117**, 127203 (2016).
[57] A. Metavitsiadis and W. Brenig, Phys. Rev. B **101**, 035103 (2020).
[58] M. Ye, R. M. Fernandes, and N. B. Perkins, Phys. Rev. Res. **2**, 033180 (2020).
[59] S. Pal, A. Seth, P. Sakrikar, A. Ali, S. Bhattacharjee, D. V. S. Muthu, Y. Singh, and A. K. Sood, arXiv:2011.00606.
[60] A. Metavitsiadis, W. Natori, J. Knolle, and W. Brenig, arXiv:2103.09828.
[61] J. Nasu, M. Udagawa, and Y. Motome, Phys. Rev. B **92**, 115122 (2015).
[62] J. Nasu, J. Yoshitake, and Y. Motome, Phys. Rev. Lett. **119**, 127204 (2017).
[63] A. Metavitsiadis, A. Pidatella, and W. Brenig, Phys. Rev. B **96**, 205121 (2017).
[64] Y. Motome and J. Nasu, J. Phys. Soc. Jpn. **89**, 012002 (2019).
[65] A. Smith, J. Knolle, D. L. Kovrizhin, and R. Moessner, Phys. Rev. Lett. **118**, 266601 (2017).
[66] M. Brenes, M. Dalmonte, M. Heyl, and A. Scardicchio, Phys. Rev. Lett. **120**, 030601 (2018).
[67] P. Karpov, R. Verdel, Y.-P. Huang, M. Schmitt, and M. Heyl, Phys. Rev. Lett. **126**, 130401 (2021).
[68] A. Smith, J. Knolle, R. Moessner, and D. L. Kovrizhin, Phys. Rev. Lett. **119**, 176601 (2017).
[69] A. Metavitsiadis and W. Brenig, Phys. Rev. B **103**, 195102 (2021).
[70] A. Pidatella, A. Metavitsiadis, and W. Brenig, Phys. Rev. B **99**, 075141 (2019).
[71] A. Metavitsiadis and W. Brenig, Rev. B **96**, 041115(R) (2017).
[72] The results of the momentum-space approach [Eq. (6)] agree to within machine precision with the real-space approach Eq. (9), using the latter for a homogeneous gauge on identical system sizes.
[73] D. Forster, *Hydrodynamic Fluctuations, Broken Symmetry, and Correlation Functions* (Benjamin, New York, 1975).
[74] The broadening is set to generate acceptably smooth spectra. For the homogeneous gauge, larger broadening has to be chosen than for the random gauge on identically sized systems, since for the former, the spectrum is more degenerate. Broadening with the random gauge has typically been set to $O(10^{-4}J)$ for the system sizes we study.